Diverging seasonal extremes for ocean acidification during the twenty-first century: Supplementary material

Lester Kwiatkowski[1*], James Orr[1]
Laboratoire des Sciences du Climat et de l'Environnement (LSCE), IPSL, CEA/CNRS/UVSQ, Orme des Merisiers, Gif-sur-Yvette, 91190, France.

1. Model evaluation

We used figures S1-S6 to evaluate the performance of the models against the Takahashi et al., (2014)[1] observation-based climatologies of carbonate chemistry variables calculated from total alkalinity, which is derived from gridded climatologies of salinity and nitrate, and pCO_2, which is based on 6.5 million observed pCO_2 data collected during 1957-2012 and adjusted to year 2005. Comparative model climatologies are constructed from the decadal mean seasonal cycle of model output from years 1995-2004.

At the global scale, modelled seasonal cycles of Ω_{arag} show higher correlation coefficients and standard deviations closer to observations than the simulated seasonal cycles of $[H^+]$, pH and pCO_2 (Fig. S1). For each of these four carbonate chemistry variables, the zonal-mean component of the modelled seasonal cycle exhibits a much higher correlation coefficient than the orthogonal zonal-anomaly component. The models also bracket the observed seasonal variance for Ω_{arag}, but they consistently overestimate that variance for $[H^+]$, pH and pCO_2. This excessive modelled seasonal variance derives from the zonal-mean component, which dominates the overall seasonal variance (Fig. S2), while the minor zonal-anomaly component is typically closer to observations (Fig. S1).

The correlation coefficients between the seasonal cycles of modelled and observed $[H^+]$ show considerable spatial variability but are generally positive. Correlation coefficients are typically highest in subtropical gyres ($r>=0.8$) and generally decline somewhat in equatorial and mid-latitude regions (Fig. S3). In contrast, correlation coefficients in the Southern Ocean are often low or even negative, confirming that in this region model skill is particularly weak, in some cases even indicating that $[H^+]$ seasonality is anticorrelated with observations. The GFDL, IPSL and CNRM-ESM1 models are particularly poor in this regard. The standard deviation of the seasonal cycle of $[H^+]$ is generally closest to observations in the low-to-mid latitudes (Fig. S4). In the higher latitudes, particularly in the Southern Ocean, models either overestimate the standard deviation of $[H^+]$ seasonal cycles (e.g. MPI-ESM-LR, MPI-ESM-MR and CNRM-ESM1) or underestimate it (e.g. GFDL and IPSL models). As mentioned in the manuscript, the poor model performance at capturing $[H^+]$ seasonality in the Southern Ocean may result from underestimated winter convective CO_2 entrainment and the impact of biological CO_2 uptake[2].

The correlation between the modelled and observed seasonal cycles of Ω_{arag} are consistently higher and show less spatial variability than those of $[H^+]$, indicating similar seasonal phasing (Fig. S5). Models have correlation coefficients of r>=0.8 globally, with the exception of generally patchier equatorial regions and lower correlations in the Southern Ocean for the MPI-ESM models (r=0.4-0.6). The standard deviation of the seasonal cycle of Ω_{arag} is generally closest to observations in the low-to-mid latitudes (Fig. S6). In the Southern Ocean, the two MPI-ESM models greatly overestimate seasonal Ω_{arag} variability while the two IPSL models tend to underestimate it. The HadGEM2-ES model largely underestimates seasonal Ω_{arag} variability in the low-to-mid latitudes and in the Arctic Ocean.

2. Future changes in diurnal variability

For insight into how future diurnal variability in $[H^+]$ may be amplified, we use data from Kerrison et al. (2011)[3] at two adjacent stations at Ischia Island in the Bay of Naples, one representing ambient conditions (Station A) and another representing a perturbation to those ambient conditions due to nearby natural venting of volcanically derived CO_2 from the seafloor (Station B). At each station, pH data loggers were installed at the surface and on the shallow seabed (~3 m), providing pH measurements every minute over periods of several days. Measurements of total alkalinity, salinity, and temperature were also made at these sites, thereby permitting calculation of the suite of carbonate system variables. Kerrison et al. summarize the mean state and diurnal variability at each station for measured pH and calculated carbonate chemistry variables, both at the surface and on the seabed.

Surface and seabed pH at the perturbed Station B are each reduced by about 0.3 relative to the ambient conditions at Station A (Table S2). That change is roughly equivalent to what is expected for open-ocean surface waters between the present day and the end of the twenty-first century under the RCP8.5 scenario. The sign and magnitude of the change in $[H^+]$ diurnal variability that we calculated from the Kerrison et al., pH data, i.e., more than doubling at Station B relative to Station A, are consistent with our analysis of future amplification of the seasonal cycle in $[H^+]$ projected by the CMIP5 models. Furthermore, the diurnal amplitude of Ω_{arag} is attenuated at Station B relative to Station A by about the same amount as seen for our estimates of the future change in the seasonal amplitude of Ω_{arag} (Table S2). For $[H^+]$ as well as Ω_{arag}, the consistency between these results on the diurnal cycle versus those on the seasonal cycle suggest that their relative changes will be similar during this century.

Table S1. The CMIP5 multi-model ensemble. The models and corresponding simulations used in this study are from Phase 5 of the Coupled Model Intercomparison Project (CMIP5). All models are Earth System Models, which include coupled ocean biogeochemistry schemes.

Model name	Model abbreviation	Simulations				
		historical	RCP8.5	1pctCO2	esmFixClim1	esmFdbk1
Community Earth System Model version 1 biogeochemistry	CESM1-BGC[4,5]	✔	✔	✖	✖	✖
Centre National de Recherches Météorologiques Earth System Model Coupled Model version 5	CNRM-ESM1[6]	✔	✔	✖	✖	✖
Geophysical Fluid Dynamics Laboratory Earth System Model version 2G	GFDL-ESM2G[7]	✔	✔	✖	✖	✖
Geophysical Fluid Dynamics Laboratory Earth System Model version 2M	GFDL-ESM2M[7]	✔	✔	✔	✔	✔
Hadley Centre Global Environment Model version 2- Earth System	HadGEM2-ES[8]	✔	✔	✖	✖	✖
Institut Pierre Simon Laplace Coupled Model version 5A-LR	IPSL-CM5A-LR[9]	✔	✔	✔	✔	✔
Institut Pierre Simon Laplace Coupled Model version 5A-MR	IPSL-CM5A-MR[9]	✔	✔	✖	✖	✖
Max-Planck-Institut für Meteorologie Earth System Model LR version	MPI-ESM-LR[10]	✔	✔	✔	✔	✔
Max-Planck-Institut für Meteorologie Earth System Model MR version	MPI-ESM-MR[10]	✔	✔	✖	✖	✖

Table S2. In situ evidence of amplification and attenuation of diurnal carbonate chemistry variability in a high-CO_2 world. The mean state and diurnal variability (Δ) of pH, $[H^+]$, pCO_2 and Ω_{arag} at two adjacent stations in the Bay of Naples. One site represents ambient conditions (Station A) while the other is adjacent to natural venting of volcanically derived CO_2 from the seafloor (Station B). The $[H^+]$, $\Delta[H^+]$, and amplification values are calculated here; all other values are taken from Kerrison et al., (2011). The amplification is computed as 100(B –A)/A.

	pH	**ΔpH**	**$[H^+]$ (nmol/kg)**	**$\Delta[H^+]$ (nmol/kg)**	**pCO_2 (µatm)**	**ΔpCO_2 (µatm)**	**Ω_{arag}**	**$\Delta\Omega_{arag}$**
Surface								
Station A	8.38	0.09	4.17	0.86	154	44	6.00	0.84
Station B	8.08	0.10	8.32	1.95	382	103	3.67	0.67
Amplification		+11%		+122%		+134%		-20%
Benthic								
Station A	8.16	0.04	6.92	0.64	300	29	4.24	0.33
Station B	7.84	0.05	14.45	1.66	734	106	2.32	0.26
Amplification		+25%		+161%		+265%		-21%

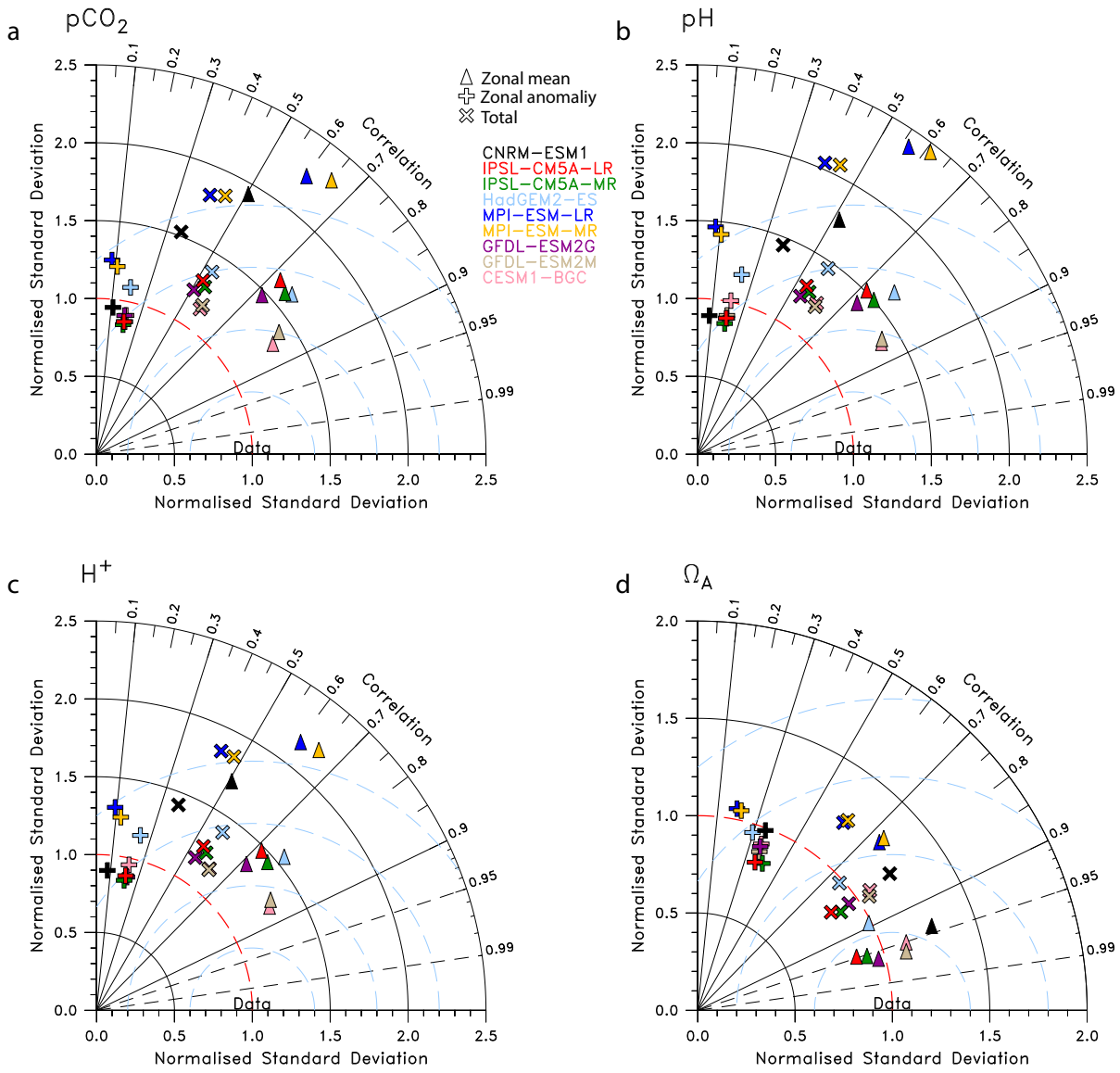

Figure S1. Taylor diagrams to evaluate seasonal variations in [H^+], pH, Ω_{arag} and pCO_2. Colours designate individual models and shapes designate the space-time components. The total seasonal component (x) is computed from monthly maps of temporal deviations (monthly means minus annual mean). That total is then separated into 2 orthogonal components: (1) triangles: zonal-mean component (monthly zonal mean minus annual zonal mean) and (2) pluses: zonal-anomaly component (maps of monthly deviations minus the zonal monthly means). This separation follows the approach of Gleckler et al. (2008)[11] for the mean square error. The observation-based reference datasets are from Takahashi et al. (2014).

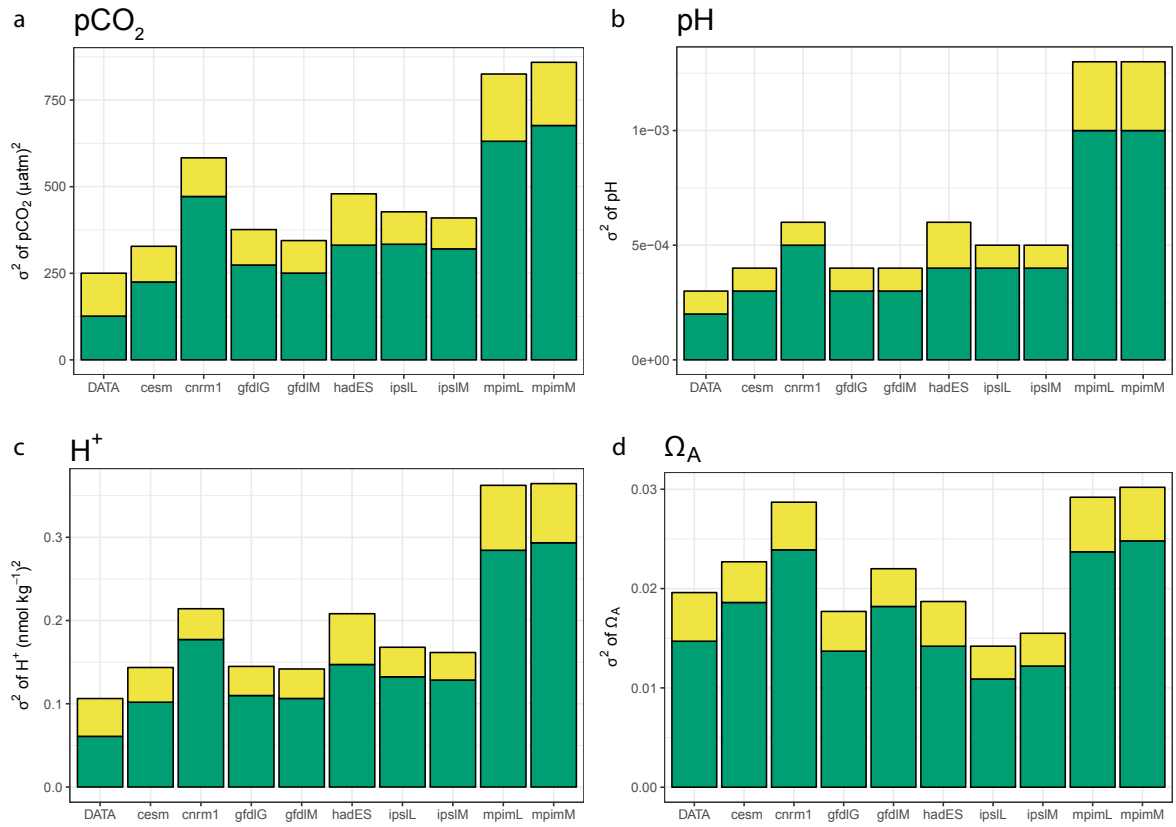

Figure S2. Modelled and observed temporal variance of pCO_2, pH, $[H^+]$ and Ω_{arag}. The total temporal variance of **a**, pCO_2, **b**, pH, **c**, $[H^+]$ and **d**, Ω_{arag} seasonal cycles divided as in Fig. S1 into zonal means (green) and zonal anomalies (yellow) for each model and the Takahashi et al. 2014 data reference (DATA). This separation follows the approach of Gleckler et al., (2008)[11] for the mean square error.

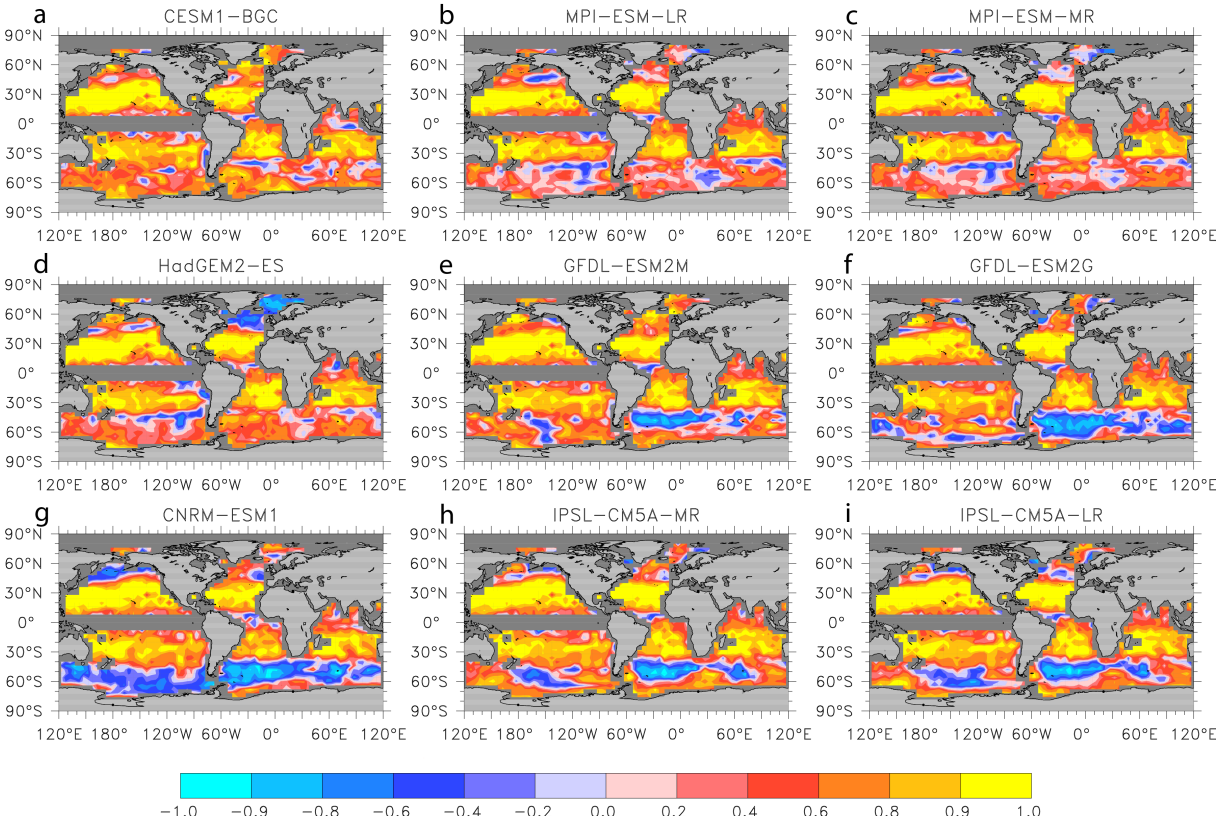

Figure S3. Correlation coefficients for the seasonal cycle of [H^+]. Maps of the temporal correlation coefficient r (over 12 months) for the climatological seasonal cycle of [H^+] between each model and the Takahashi et al., 2014 data reference. Global area-weighted means of these results are shown as the total component (x) in Fig. S1c. Climatological values in the equatorial Pacific region are not provided in the observational data reference due to total alkalinity exhibiting large interannual variability associated with El Niño events.

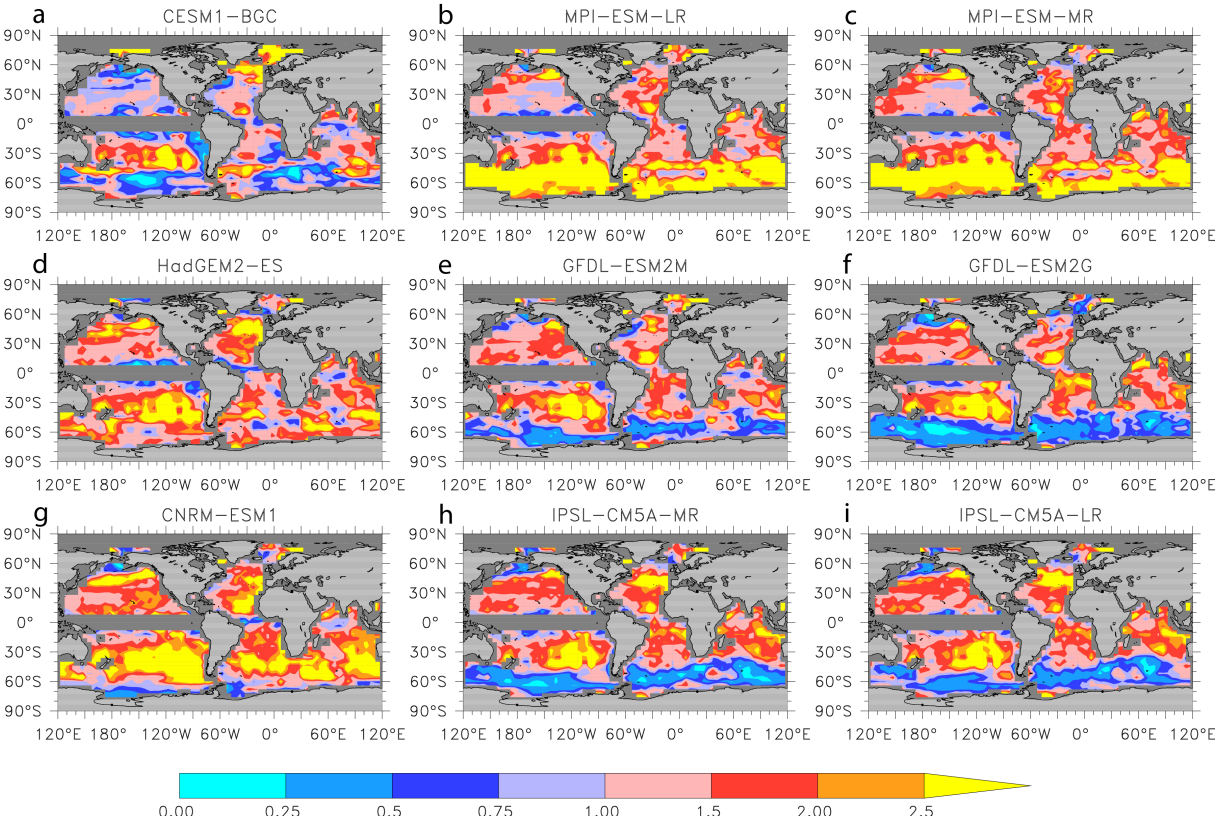

Figure S4. The normalised standard deviation of the seasonal cycles of [H^+]. Maps from each model for the standard deviation of seasonal cycle of [H^+] normalised by dividing by the corresponding standard deviation of the Takahashi et al., 2014 data reference. That is, values >1 represent simulated seasonal variability that is greater than the data-based climatology, while values <1 represent areas where it is lower. Global area-weighted means of these results are shown as the total component (x) in Fig. S1c.

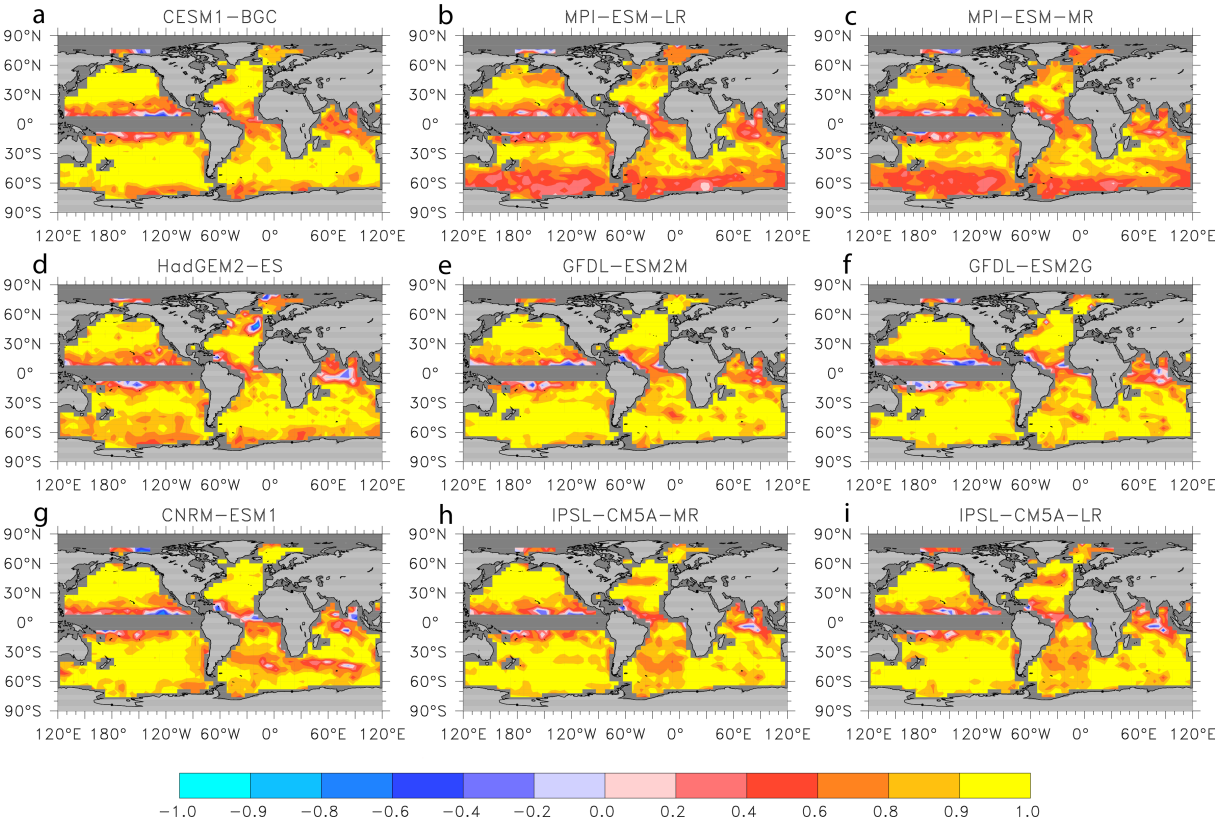

Figure S5. Correlation coefficients for the seasonal cycle of Ω_{arag}. Maps of the temporal correlation coefficient r (over 12 months) for the climatological seasonal cycle of Ω_{arag} between each model and the Takahashi et al. (2014) data reference. Global area-weighted means of these results are shown as the total component (x) in Fig. S1d.

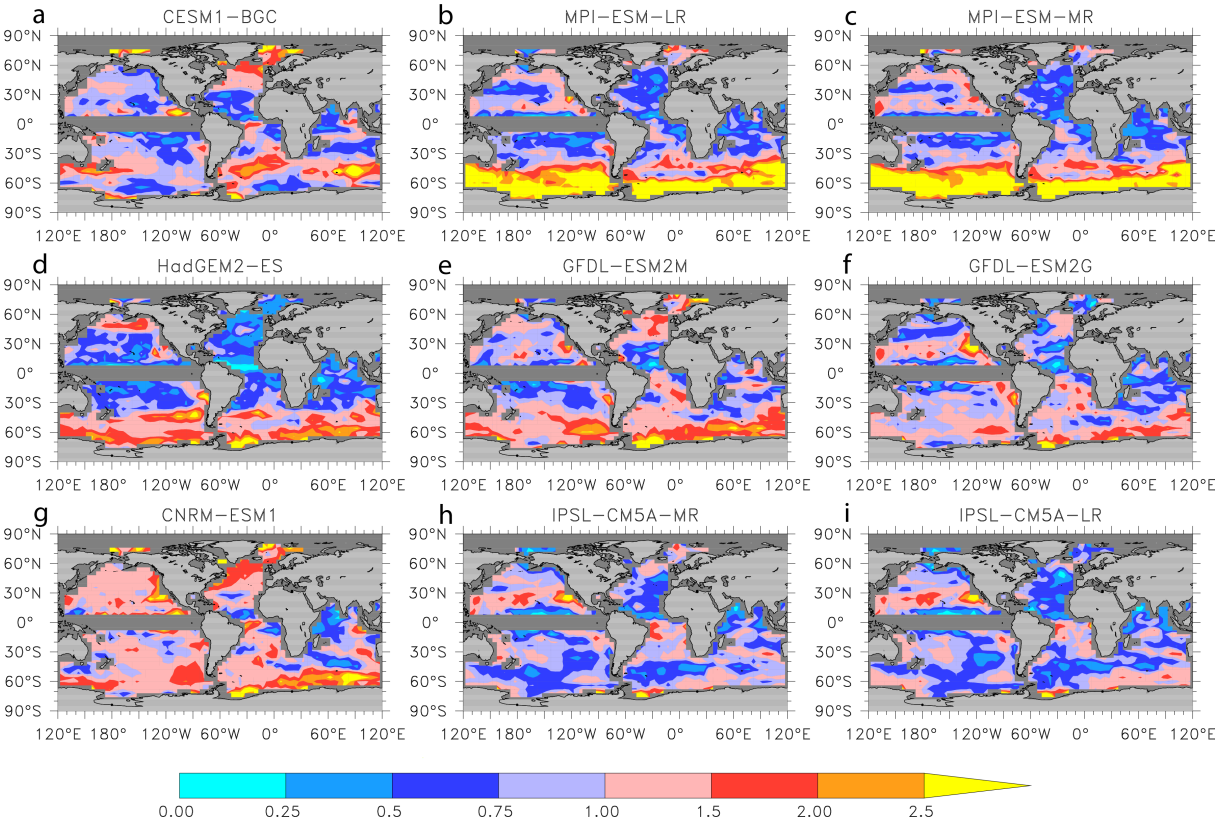

Figure S6. The normalised standard deviation for the seasonal cycle of Ω_{arag}. Maps from each model for the standard deviation of monthly climatological Ω_{arag} normalised by dividing by the corresponding standard deviation for the Takahashi et al. (2014) data reference. Global area-weighted means of these results are shown as the total component (x) in Fig. S1d.

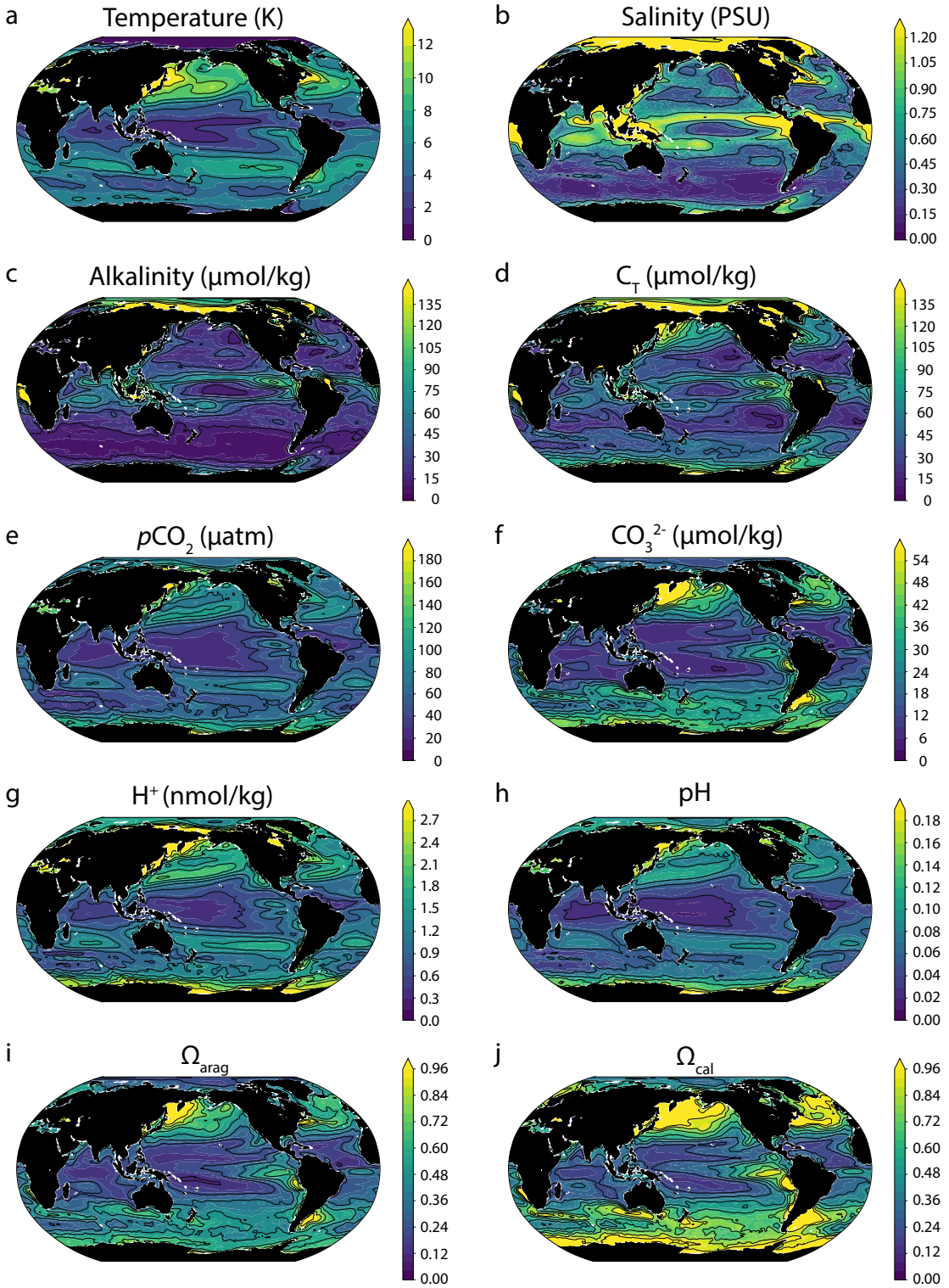

Figure S7. Seasonal amplitude of carbonate chemistry variables, temperature and salinity. The multi-model mean seasonal amplitudes of **a**, temperature, **b**, salinity, **c**, total alkalinity, **d**, dissolved inorganic carbon (C_T), **e**, pCO_2, **f**, CO_3^{2-}, **g**, $[H^+]$, **h**, pH, **i**, Ω_{arag} and **j**, Ω_{cal} in the 1990s.

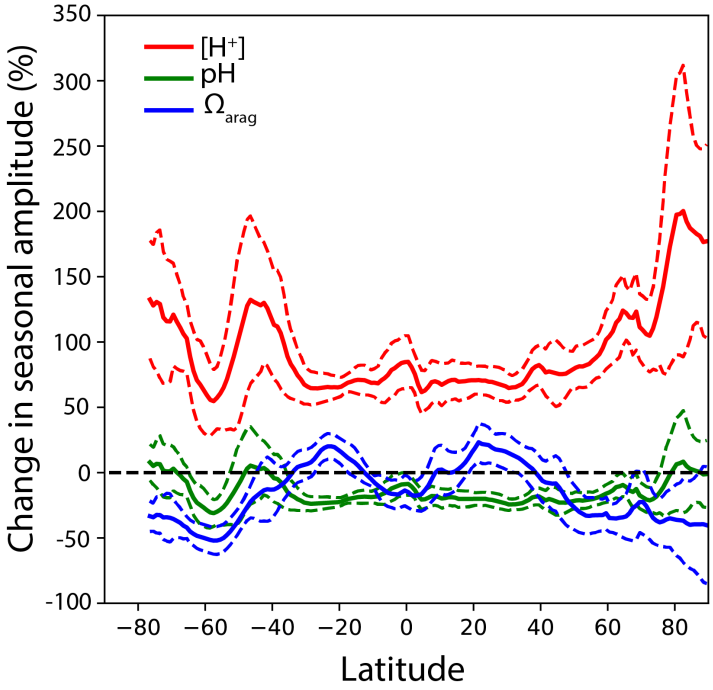

Figure S8. Zonal-mean changes in seasonal amplitude of selected carbonate chemistry variables over the twenty-first century. The zonal-mean changes in the seasonal amplitude of $[H^+]$, pH and Ω_{arag} in the 2090s relative to the 1990s based on the historical and RCP8.5 CMIP5 simulations. Multi-model means (solid lines) are shown with ± 1 standard deviation (dashed lines).

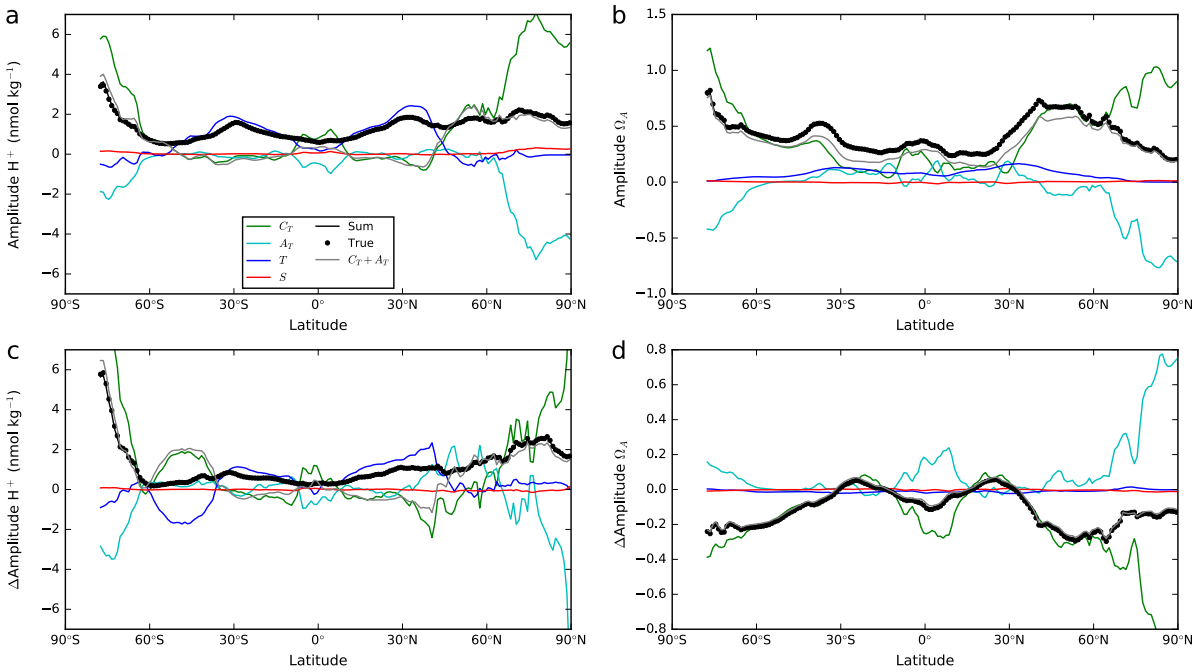

Figure S9. Drivers affecting seasonal amplitudes of [H$^+$] and Ω_{arag} in the RCP8.5 simulation of the GFDL-ESM2M model. The influence of C_T, A_T, T and S on the seasonal amplitude of [H$^+$] and Ω_{arag} for the 2006-2015 mean (**a, b**) and the change in seasonal amplitude of [H$^+$] and Ω_{arag} between averages for 2006-2015 and 2091-2100 (**c, d**). Each coloured line represents one of the four product-terms on the right hand side of Equation 2, each consisting of a partial differential times a delta value (e.g., $(\partial y/\partial C_T)\Delta C_T$). The grey line represents the sum of the C_T and A_T terms. The black line represents the sum of all 4 terms, while the black dots represent the actual change in the derived variable. The former and latter overlap, indicating that this decomposition accurately reproduces changes in the seasonal amplitude of [H$^+$] and Ω_{arag}.

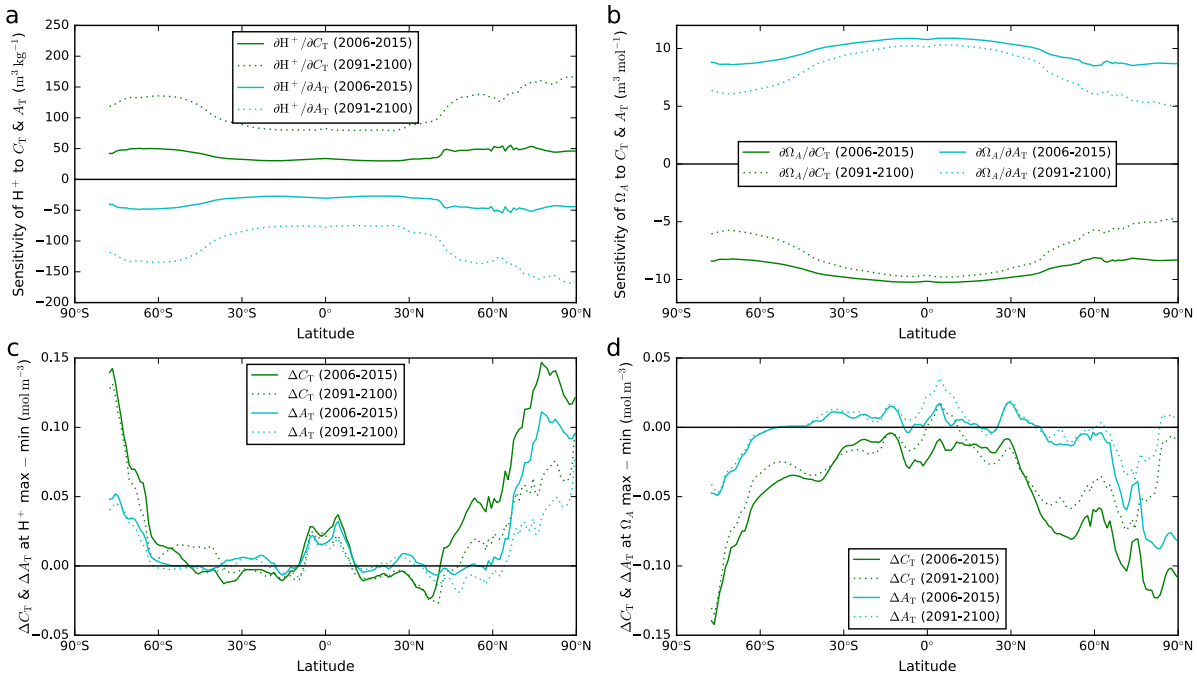

Figure S10. Decomposition of C_T and A_T terms in Equation 2 into sensitivities and amplitude changes for [H$^+$] and Ω_{arag} in the RCP8.5 simulation of the GFDL-ESM2M model. The zonal-mean sensitivities of **a**, [H$^+$] and **b**, Ω_{arag} to C_T and A_T shown as means for 2006-2015 and 2091-2100 along with the corresponding zonal-mean ΔC_T and ΔA_T taken between monthly maximum and minimum for **c**, [H$^+$] and **d**, Ω_{arag}.

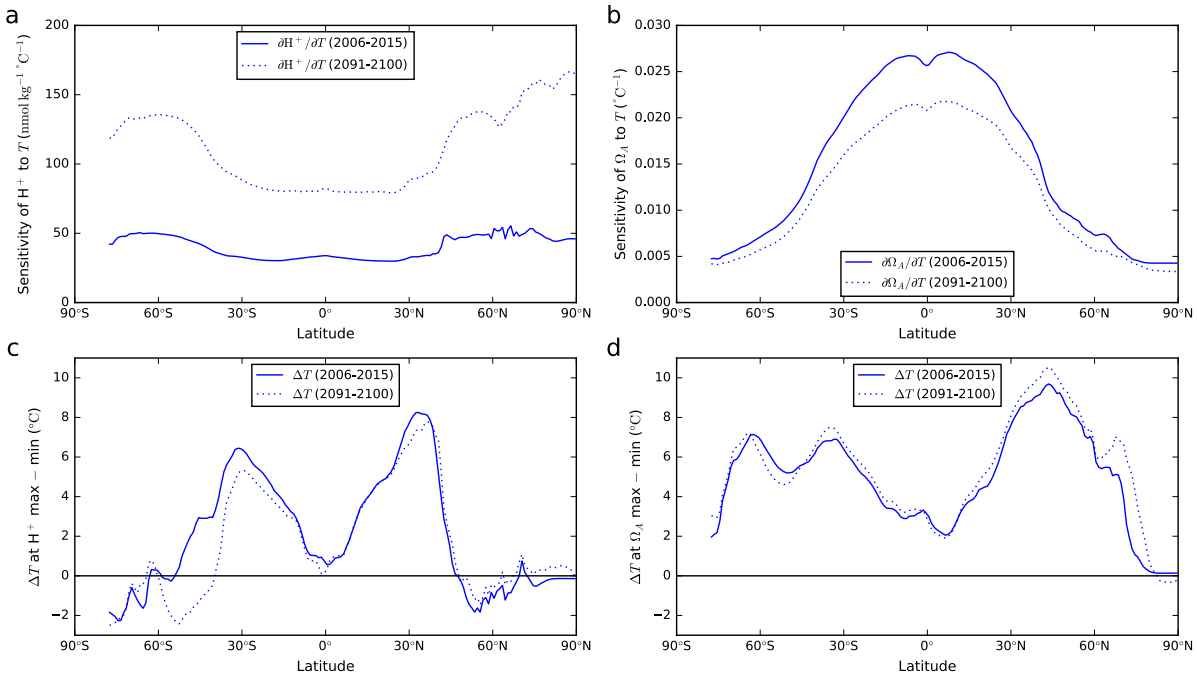

Figure S11. Decomposition of the T term in Equation 2 into sensitivities and amplitude changes for both [H^+] and Ω_{arag} in the RCP8.5 simulation of the GFDL-ESM2M model. The zonal-mean sensitivities of **a**, [H^+] and **b**, Ω_{arag} to temperature shown as means for 2006-2015 and 2091-2100 along with the corresponding zonal-mean ΔT taken between monthly maximum and minimum for **c**, [H^+] and **d**, Ω_{arag}.

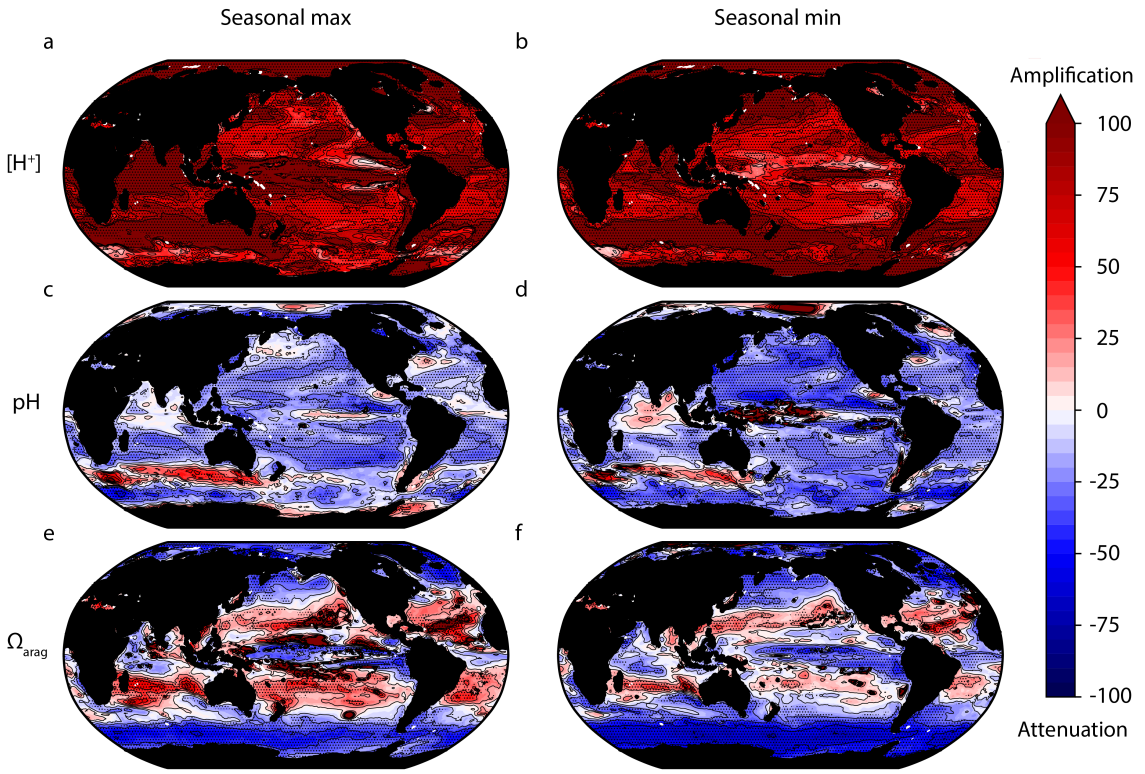

Figure S12. The twenty-first century change in seasonal maxima and minima for [H^+], pH and Ω_{arag}. The multi-model mean anomaly (%) in the seasonal maximum and minimum of [H^+], pH and Ω_{arag} between decadal means for the 2090s and those for the 1990s. Stippling shows areas of high confidence as determined by model sign agreement with a standard of 8 out of 9 models representing significance.

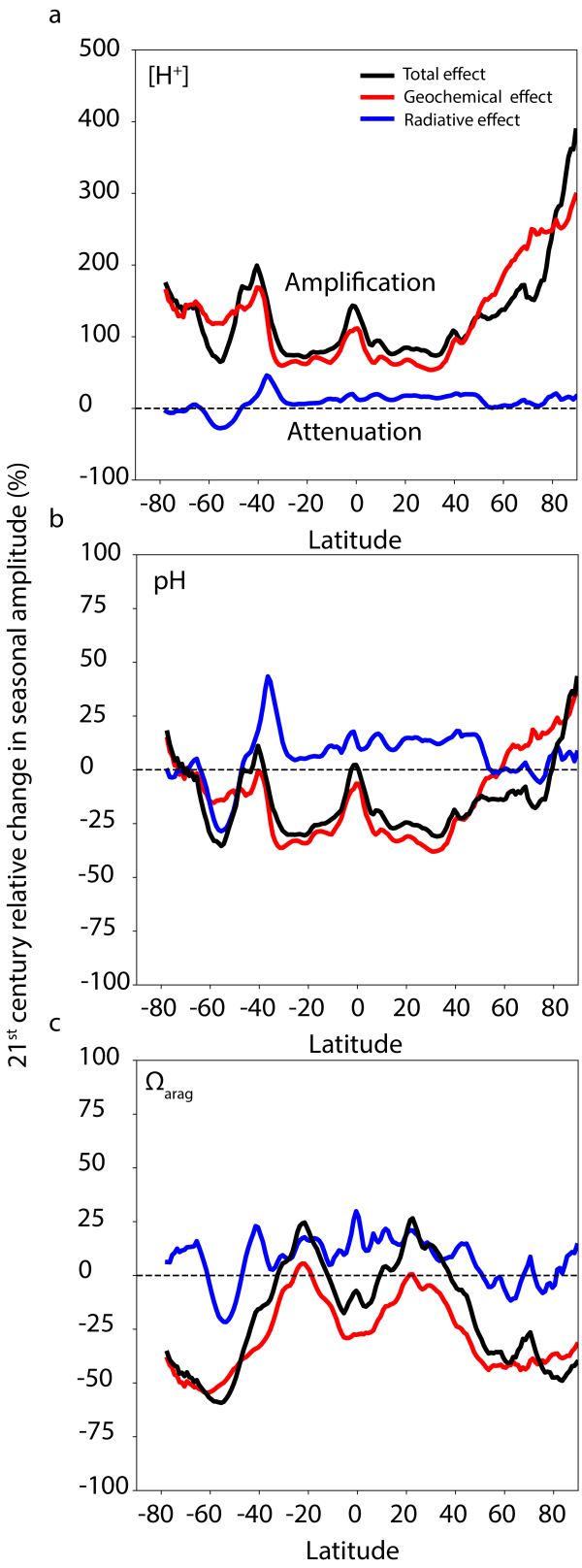

Figure S13. Contributions of geochemical and radiative effects of atmospheric CO_2 to zonal-mean seasonal amplitude changes. The multi-model zonal-mean anomaly (%) in the seasonal amplitude of **a**, $[H^+]$ **b**, pH and **c**, Ω_{arag} under CO_2 and climate feedback forcing (black lines), CO_2 only forcing (red lines) and climate feedback only forcing (blue lines). Anomalies are calculated as the relative difference between the last decade of simulations (years 131-140) minus the first decade (years 1-10).

References

1. Takahashi, T. *et al.* Climatological distributions of pH, pCO2, total CO2, alkalinity, and CaCO3 saturation in the global surface ocean, and temporal changes at selected locations. *Mar. Chem.* **164,** 95–125 (2014).
2. Mongwe, N. P., Chang, N. & Monteiro, P. M. S. The seasonal cycle as a mode to diagnose biases in modelled CO2 fluxes in the Southern Ocean. *Ocean Model.* **106,** 90–103 (2016).
3. Kerrison, P., Hall-Spencer, J. M., Suggett, D. J., Hepburn, L. J. & Steinke, M. Assessment of pH variability at a coastal CO2 vent for ocean acidification studies. *Estuar. Coast. Shelf Sci.* **94,** 129–137 (2011).
4. Gent, P. R. *et al.* The Community Climate System Model Version 4. *J. Clim.* **24,** 4973–4991 (2011).
5. Lindsay, K. *et al.* Preindustrial-Control and Twentieth-Century Carbon Cycle Experiments with the Earth System Model CESM1(BGC). *J. Clim.* **27,** 8981–9005 (2014).
6. Voldoire, A. *et al.* The CNRM-CM5.1 global climate model: description and basic evaluation. *Clim. Dyn.* **40,** 2091–2121 (2012).
7. Dunne, J. P. *et al.* GFDL's ESM2 Global Coupled Climate–Carbon Earth System Models. Part I: Physical Formulation and Baseline Simulation Characteristics. *J. Clim.* **25,** 6646–6665 (2012).
8. Collins, W. J. *et al.* Development and evaluation of an Earth-System model - HadGEM2. *Geosci. Model Dev.* **4,** (2011).
9. Dufresne, J.-L. *et al.* Climate change projections using the IPSL-CM5 Earth System Model: from CMIP3 to CMIP5. *Clim. Dyn.* **40,** 2123–2165 (2013).
10. Giorgetta, M. A. *et al.* Climate and carbon cycle changes from 1850 to 2100 in MPI-ESM simulations for the Coupled Model Intercomparison Project phase 5. *J. Adv. Model. Earth Syst.* **5,** 572–597 (2013).
11. Gleckler, P. J., Taylor, K. E. & Doutriaux, C. Performance metrics for climate models. *J. Geophys. Res. Atmospheres* **113,** D06104 (2008).